p-Si/SnO_2/Fe_2O_3 Core/Shell/Shell Nanowire Photocathodes for Neutral pH Water Splitting

*Alireza Kargar, Sung Joo Kim, Paniz Allameh, Chulmin Choi, Namseok Park, Huisu Jeong, Yusin Pak, Gun Young Jung, Xiaoqing Pan, Deli Wang, and Sungho Jin**

Silicon is one of the promising materials for solar water splitting and hydrogen production; however, it suffers from two key factors, including the large external potential required to drive water splitting reactions at its surface and its instability in the electrolyte. In this study, a successful fabrication of novel p-Si/n-SnO_2/n-Fe_2O_3 core/shell/shell nanowire (css-NW) arrays, consisting of vertical Si NW cores coated with a thin SnO_2 layer and a dense Fe_2O_3 nanocrystals (NCs) shell, and their application for significantly enhanced solar water reduction in a neutral medium is reported. The p-Si/n-SnO_2/n-Fe_2O_3 css-NW structure is characterized in detail using scanning, transmission, and scanning transmission electron microscopes. The p-Si/n-SnO_2/n-Fe_2O_3 css-NWs show considerably improved photocathodic performances, including higher photocurrent and lower photocathodic turn-on potential, compared to the bare p-Si NWs or p-Si/n-SnO_2 core/shell NWs (cs-NWs), due to increased optical absorption, enhanced charge separation, and improved gas evolution. As a result, photoactivity at 0 V versus reversible hydrogen electrode and a low onset potential in the neutral solution are achieved. Moreover, p-Si/n-SnO_2/n-Fe_2O_3 css-NWs exhibit long-term photoelectrochemical stability due to the Fe_2O_3 NCs shell well protection. These results reveal promising css-NW photoelectrodes from cost-effective materials by facile fabrication with simultaneously improved photocathodic performance and stability.

A. Kargar, P. Allameh, N. Park, Prof. D. Wang
Department of Electrical and Computer Engineering
University of California–San Diego
La Jolla, CA 92093, USA
S. J. Kim, Prof. X. Pan
Department of Materials Science and Engineering
University of Michigan
Ann Arbor, MI 48109, USA
Dr. C. Choi, Prof. D. Wang, Prof. S. Jin
Materials Science and Engineering Program
University of California–San Diego
La Jolla, CA 92093, USA
E-mail: jin@ucsd.edu
Dr. C. Choi, Prof. S. Jin
Department of Mechanical and Aerospace Engineering
University of California–San Diego
La Jolla, CA 92093, USA
H. Jeong, Y. Pak, Prof. G. Y. Jung
School of Materials Science and Engineering
Gwangju Institute of Science and Technology (GIST)
Buk-gu, Gwangju 500–712, South Korea
Prof. D. Wang
Qualcomm Institute (QI)
University of California–San Diego
La Jolla, CA 92093, USA

DOI: 10.1002/adfm.201404571

1. Introduction

Silicon is the most widely used semiconductor for solar cells[1–4] and has also shown promising performances in photoelectrochemical (PEC) cells for hydrogen production.[5–10] Silicon photoelectrodes with nano/micro structures such as nano/micro wire array[9,11] and black silicon[7] have exhibited improved PEC performances. Silicon nanowire (NW) arrays, in particular, are of considerable interest due to their distinctive properties, facile and scalable techniques for their fabrication, etc.[11–19] On the other hand, there are two key factors limiting the application of silicon photoelectrodes for practical solar hydrogen generation including their large external biasing potential (high overpotential) required to drive hydrogen or oxygen evolution reaction (HER or OER) and their instability in the electrolyte. Tremendous efforts have been expended to overcome these limiting factors such as using metal catalysts (noble[20,21] or non-noble[22–24]) to reduce the turn-on (or onset) potential and by coating the electrodes surface with a corrosion-resistant layer such as TiO_2[25–27] for stability improvement. A thin TiO_2 coating layer can significantly enhance the stability,[27] however due to its poor conductivity, a metal co-catalyst needs to be deposited on its surface to boost the HER or OER.[25,26]

Therefore, a more functional metal oxide coating layer, which can simultaneously enhance the PEC performance and HER/OER kinetics, and electrode stability, is desirable. Recent studies have demonstrated that chemical-vapor and atomic-layer deposited Fe_2O_3,[17,28] atomic layer-deposited MnO,[29] and sputtered $NiRuO_x$,[30] thin layers can considerably improve the photoanodic performance and OER kinetics of n-Si photoanodes, while also enhancing the n-Si stability. On the other hand, less attention has been paid to the application of a functional metal oxide layer on the p-Si photocathodes to concurrently enhance the photocathodic performance and HER kinetics and p-Si stability. There are reports for coating of p-Si photocathodes with different metal oxides such as SnO_2,[31] TiO_2,[32] ITO,[33] WO_3,[34] FeO_x,[35] etc., however none of them are efficient in both enhanced performance and stability. The metal oxide coating layer can also be in the form of a nanostructure increasing the reaction surface area. We have recently

shown that growing ZnO NWs on the p-Si NW cores enhance the photocathodic performance, however they cannot stabilize the p-Si NWs for a long time.[36] Moreover, to facilitate the overall spontaneous solar water splitting, a low photocathodic onset potential is required.

Fe_2O_3 (α phase: hematite), an n-type semiconductor with a bandgap of ≈2.1 eV absorbing the visible light is chemically stable in an aqueous medium, is made from abundant and low-cost elements, and environmentally friendly.[37–39] Moreover, the hematite nanostructures can be synthesized in large scales using facile and cost-effective methods such as hydrothermal growth technique.[40–42] These properties make hematite of particular interest to couple with the p-Si NW photocathodes. On the other hand, hematite suffers from several drawbacks[37,43] including short hole diffusion length (2–4 nm),[44] short light penetration length,[45] short excited-state carrier lifetime,[46] poor gas evolution reaction kinetics,[37] low carrier mobility[47,48] (both electron and hole mobilities are low but electron mobility is higher than hole mobility[49]), and surface trapping states.[50] Consequently, the PEC performance of hematite is morphology dependent.[37,51]

Herein, to improve the photocathodic performance and HER kinetics of p-Si NWs and simultaneously to enhance the p-Si stability, we grew dense Fe_2O_3 nanocrystals (NCs) (forming a shell) on the patterned and dry-etched 3D p-Si NW arrays pre-coated with a thin SnO_2 seeding layer (this structure is called "p-Si/n-SnO_2/n-Fe_2O_3 core/shell/shell nanowires (css-NWs)") using an easily scalable hydrothermal synthesis method. The morphology and atomic structure of the css-NWs are studied in detail. The css-NWs' PEC performances including photocurrent and PEC stability are investigated and presented. Moreover, the effects of Si NW length and electrolyte pH on the PEC performance are evaluated.

2. Results and Discussion

Figure 1a–c shows the top-view and cross-sectional scanning electron microscopy (SEM) images of bare p-Si NW array etched for 10 min (denoted 10m-Si NW). The center-to-center spacing (pitch size) is 1 μm, the average Si etching rate is ≈0.24 μm min^{-1}, and the diameters are ≈330 nm and ≈280 nm (see Figure 1c) for 5 and 10 min etching times, respectively. Note that the p-Si NWs were made from the same nanoimprinting mold; thus, the difference in diameter after different etching times is due to the Reactive Ion Etching-Inductively Coupled Plasma (RIE-ICP) etching process.[36] The p-Si NWs in this study were made from p-Si(100) and p-Si(111) wafers denoting with p-Si(100) and p-Si(111) NWs, respectively (see the Experimental Section for details). Note that unless otherwise stated, the p-Si orientation is (100). For convenience, p-Si/SnO_2/Fe_2O_3 css-NWs for Fe_2O_3 NCs grown for 2 h and different p-Si NW core etching times are denoted as "css(Xm-Si/SnO_2/2h-Fe_2O_3) NWs", in which "X" is the p-Si NW etching time in minutes (min). The SEM images of css(5m-Si/SnO_2/2h-Fe_2O_3) NWs are shown in Figure 1d–f. Formation of the Si/SnO_2/Fe_2O_3 css-NWs is within the whole area of samples (this was investigated for different parts on the samples), which can be realized and seen by the low-magnification SEM images (Figure 1d,e). The Fe_2O_3 NCs cover the whole length of Si NW core surface as well as the spaces between Si NWs on the flat surface (see Figure 1f) due to uniform coverage of SnO_2 seeding layer (see the Experimental Section for uniform coating). Figure 1g–j exhibits the SEM images of the css(10m-Si/SnO_2/2h-Fe_2O_3) NWs revealing the similar observation of uniform growth of the Fe_2O_3 NCs on the entire length of Si NWs. The average diameter and length of Fe_2O_3 NCs on 10m-Si NW cores are ≈37 nm and ≈136 nm, respectively (see Figure 1h,j). Using the Fe_2O_3 NCs compared to the Fe_2O_3 NWs can assist to minimize/overcome some of the Fe_2O_3 limiting factors especially the short diffusion length issue, leading to increased photogenerated carrier transport. The cross-sectional SEM images, shown in Figure 1i,j, exhibit different regions including Si substrate, thin SnO_2 seeding layer (thickness of ≈28 nm), and Fe_2O_3 NCs (average length of ≈136 nm). These interfaces on the surface of Si NW backbone will be further shown in the transmission electron microscopy (TEM) images.

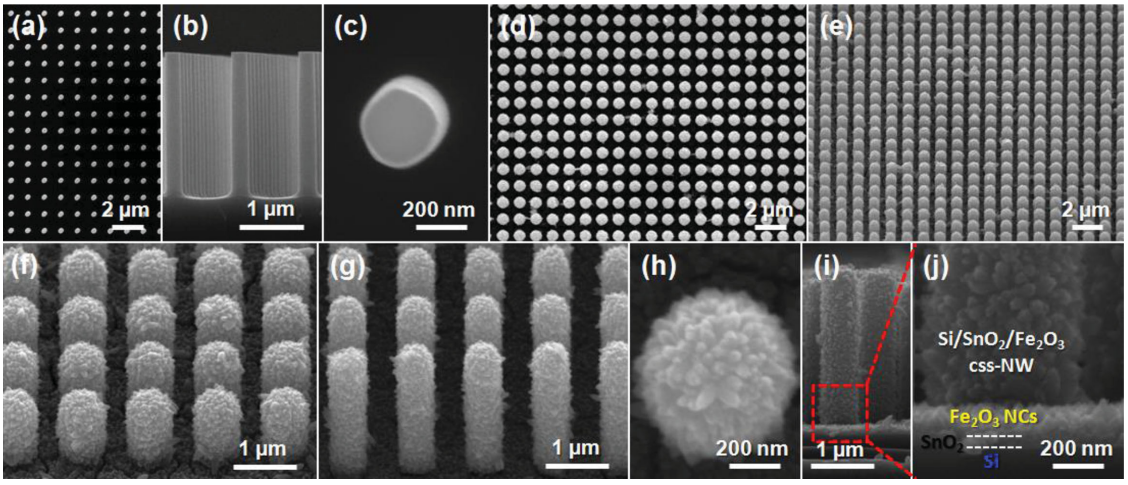

Figure 1. SEM images of Si/SnO_2/Fe_2O_3 css-NW arrays. a–c) Top-view (low magnification), cross-sectional and top-view (high magnification) images of bare 10m-Si NW array. d–f) Top-view and 45° view images (with two different magnifications) of css(5m-Si/SnO_2/2h-Fe_2O_3) NWs. g–j) 45° view, top-view and cross-sectional images of css(10m-Si/SnO_2/2h-Fe_2O_3) NWs.

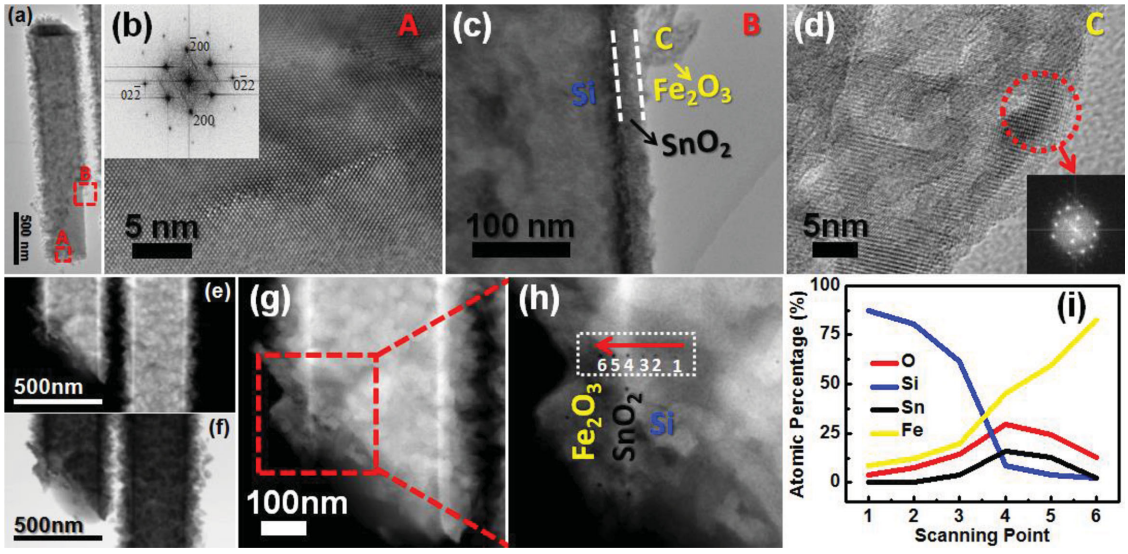

Figure 2. a) TEM image of a single css(20m-Si/SnO_2/2h-Fe_2O_3) NW broken from the substrate in its length. b) HRTEM image of labeled area "A" in a) exhibiting the crystal structure of Si NW core. Inset exhibits the calculated FFT pattern. c) High-magnification TEM image of labeled area "B" in a) showing the interfaces among Si, SnO_2, and Fe_2O_3. d) HRTEM image of labeled Fe_2O_3 NC ("C") in c). Inset shows the calculated FFT pattern of selected area. Low-magnification annular e) dark and f) bright field STEM images of two broken single css(20m-Si/SnO_2/2h-Fe_2O_3) NWs. g) High angle annular dark field STEM image of the left css-NW in e). h) Higher magnification high angle annular dark field STEM image of labeled area in g). i) EDS point scan taken along the interfaces of Si, SnO_2, and Fe_2O_3 (points indicated in h)).

TEM image of a single css(20m-Si/SnO_2/2h-Fe_2O_3) NW is shown in **Figure 2**a. Note that the single css-NW was broken from about the middle of its length as 20m-Si NW has a length of ≈5 µm. The single crystalline Si NW core with growth along [200] orientation is demonstrated from the high-resolution TEM (HRTEM) image in Figure 2b with its calculated fast Fourier transform (FFT) pattern, in the inset, further confirms it. High-magnification TEM image (Figure 2c) clearly exhibits the interfaces among Si NW core, SnO_2 seeding layer, and Fe_2O_3 NC, which are sharp (also see Figure 2e–h) without an amorphous layer revealing the clean interfaces. The HRTEM image shown in Figure 2d exhibits a polycrystalline nature for the Fe_2O_3 NC. The FFT pattern of the labelled part of HRTEM image shows the crystal structure of a single grain of Fe_2O_3 NC. The high angle annular dark field (HAADF) scanning transmission electron microscopy (STEM) image of a broken part of the single css(20m-Si/SnO_2/2h-Fe_2O_3) NW (Figure 2g) clearly shows the existence of thin SnO_2 layer, which is within the total length of Si NW core (see Figure 2e,f). Energy dispersive X-ray spectroscopy (EDS) point scan (Figure 2i) taken along the interfaces of Si, SnO_2, and Fe_2O_3 (points indicated in Figure 2h) further exhibits the sharp interfaces between Si, SnO_2, and Fe_2O_3. Note that the atomic percentage of oxygen is expected to be low because a light element like oxygen is hard to detect in a single NW of which the scanning volume is small. Also, it is difficult to scan through the cross-section of a css-NW with individual layer-by-layer; there is a scanning overlap between Fe_2O_3 NC and SnO_2 layer, resulting in higher atomic percentage of oxygen than that from a pure Fe_2O_3 region.

Figure 3a shows the current density under illumination in a neutral solution of 10m-Si NW cores with different coatings including bare Si NWs, SnO_2-seeding-layer-coated Si NWs (Si/SnO_2 cs-NWs), and Si/SnO_2/Fe_2O_3 css-NWs, in which all the samples show photocathodic behavior. The Si/SnO_2/Fe_2O_3 css-NWs present much higher photocathodic current and significant photocathodic turn-on potential shift toward more positive

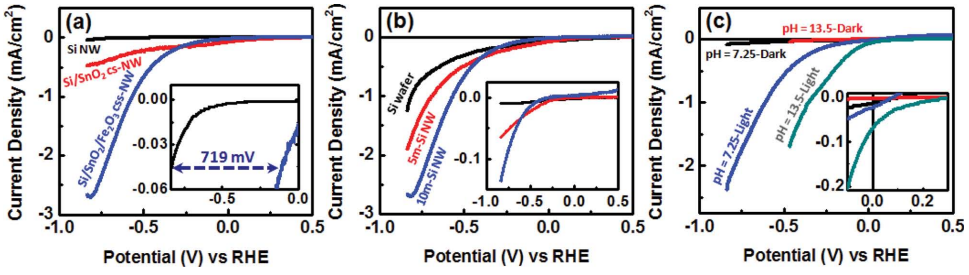

Figure 3. a) Current density under illumination of 10m-Si NW cores with different coatings (black: bare NW, red: Si/SnO_2 cs-NW, blue: Si/SnO_2/Fe_2O_3 css-NW). Inset shows the corresponding zoom-in curves with calculated potential shift. b) Current density under illumination of css(Si/SnO_2/2h-Fe_2O_3) NWs with different Si etching times. Inset shows the dark current of corresponding samples. c) Current density at dark and under illumination of css(10m-Si/SnO_2/2h-Fe_2O_3) NWs measured in two different electrolytes with different pHs (0.25 M Na_2SO_4, pH = 7.25 and 1 M NaOH, pH = 13.5). Inset shows the zoom-in curves around 0 V versus RHE.

potentials than the bare Si NWs or Si/SnO_2 cs-NWs. The potential shift is ≈719 mV compared to the bare Si NW array (Figure 3a, inset). This is an interesting feature showing that we can significantly reduce the photocathodic turn-on potential of p-Si NW photocathodes in a neutral solution using Si/metal-oxides heterojunctions without using a metal nanoparticle catalyst coating on the p-Si NWs. The improved photocathodic performance is due to the increased reaction surface area (which comes from the nanotextured shell), effective energy band alignment among p-Si, n-SnO_2, and n-Fe_2O_3 (see Supporting Information, Figures S1–S3, for the energy band diagram of the css-NW heterojunctions), enhanced optical absorption due to combination of materials with different bandgaps,[17,52] and improved gas evolution coming from the Fe_2O_3 NCs. The effective band alignment at an electrolyte pH of 7.25, as shown in Supporting Information, Figure S3, provides multiple junctions enhancing the charge separation within the css-NW. There may also be a catalyst effect from the Fe_2O_3 NCs shell contributing to the enhanced photocathodic current.[28] The Si/SnO_2 cs-NWs exhibit higher photocathodic current than the bare Si NWs due to the enhanced optical absorption and junction between p-Si and n-SnO_2 improving the charge separation.

The effect of Si NW etching time (Si NW length) on the photocathodic current of Si/SnO_2/Fe_2O_3 css-NWs is shown in Figure 3b (Si wafer is considered for zero etching time). Longer Si NW core in the NW samples results in higher photocathodic current mainly due to increased reaction surface area. The smaller diameter for longer NW backbone in the NW samples can also be an effective factor leading to lower recombination and consequently contributing to the improved photocathodic current. Note that for comparison of the NW samples with the bare Si wafer, the enhanced surface area may not be the dominant factor due to the pitch size of 1 µm. In fact, other factors coming from the advantages of vertical NW arrays (including enhanced light absorption, reduced charge recombination, improved carrier collection, and increased reaction rate) can contribute in the enhanced photocathodic performance. The dark current of corresponding samples is shown in the inset exhibiting the same trend as the photocathodic current. The Si NW array pitch size is another key factor, which can further increase the photocurrent and shift the photocathodic turn-on potential toward more positive potentials.[36] Using Si NWs with higher density and longer length, we can get higher photocurrent and a positive photocathodic turn-on (onset) potential, which we are working on that, to build a tandem PEC cell for overall solar water splitting in neutral pH water.

Another parameter affecting the PEC performance of the Si/SnO_2/Fe_2O_3 css-NWs is the type of measurement electrolyte and its pH (Figure 3c). The dark current in both neutral and basic electrolytes with pH = 7.25 and pH = 13.5, respectively, is almost the same and negligible, while the current under illumination at the basic electrolyte is much higher than that in the neutral solution. Furthermore, the basic electrolyte shifts the photocathodic turn-on potential compared to the performance in the neutral solution. However, note that for practical solar hydrogen production, a neutral medium can be more desirable as the natural water resources such as seawater are usually in a neutral condition and using a neutral solution prevents the use of strong acids and bases which can result in environmental and handling issues. As shown in Figure 3c, inset, the Si/SnO_2/Fe_2O_3 css-NWs are photoactive at 0 V versus reversible hydrogen electrode (RHE) in both neutral and basic electrolytes, which was confirmed by the current densities under chopped illumination (see Supporting Information, Figure S4). The photocurrent at 0 V versus RHE can be further enhanced by using Si NW cores with longer length and smaller pitch size as discussed above. The current densities under chopped illumination of css(5m-Si/SnO_2/2h-Fe_2O_3) and css(10m-Si/SnO_2/2h-Fe_2O_3) NWs in both neutral and basic electrolytes (Supporting Information, Figure S4) exhibit the same currents as that shown in Figure 3b,c, revealing that the high photoactivity of the css-NWs preserve under different scans. Measured incident photon-to-current efficiency (IPCE) of the css-NWs (data not shown here) exhibited a broadband absorption spectrum due to coupling of Si and Fe_2O_3 with ≈1.11 eV and ≈2.1 eV bandgaps, respectively.

Photocurrent stability tests were performed by collecting the samples current under a fixed illumination of 100 mW cm^{-2} and at a biasing potential of –0.33 V versus RHE. **Figure 4**a shows the stability test of css(8.5m-Si(111)/SnO_2/2h-Fe_2O_3) NWs in the neutral electrolyte exhibiting a constant photocurrent. Note that the Si(111) NW cores were made from slightly larger diameter nanoimprinting substrates resulting in different etching rate compared to that of the Si(100) NWs (see the Experimental Section for more details), in which the 8.5m-Si(111) NWs have similar length to that of the 10m-Si(100) NWs (the pitch size is also the same). Note that the photocurrent first starts increasing

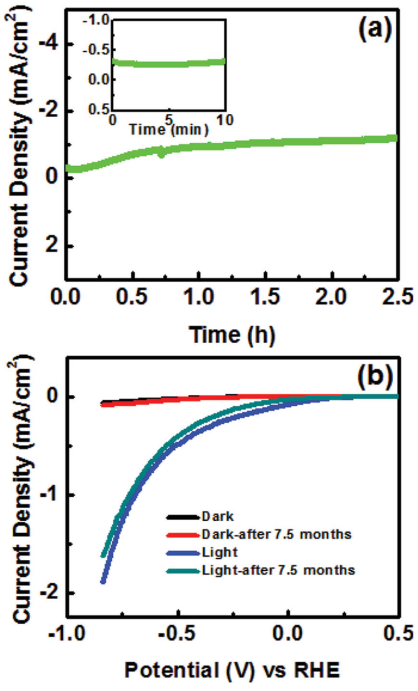

Figure 4. a) Current density under constant light illumination versus time (stability performance) of css(8.5m-Si(111)/SnO_2/2h-Fe_2O_3) NWs in neutral electrolyte measured at –0.33 V versus RHE. Inset shows the enlarged first part (0–10 min) of the current density. b) Current density at dark and under illumination of css(5m-Si/SnO_2/2h-Fe_2O_3) NWs measured in two different times (the sample was kept in vacuum and retested after 7.5 months).

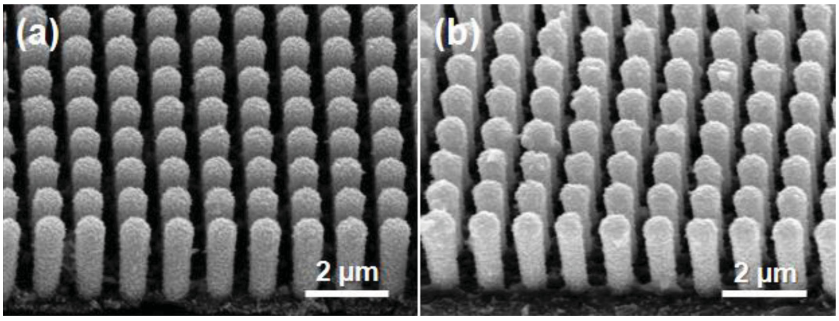

Figure 5. a) SEM images of css(8.5m-Si(111)/SnO_2/2h-Fe_2O_3) NW photoelectrode before PEC and stability tests (as-fabricated sample), and b) after PEC tests and a long stability test of over 6 h.

until it reaches its plateau/saturation and after that, it remains constant, similar to that reported for the TiO_2/Ir-coated n-Si photoanodes[25] or TiO_2/Pt-coated ZnO/Si branched NW photocathodes.[26] The reason for the observed current increase initially and then reaching a plateau/saturation is not totally clear at this point and is under investigation. Note also that the beginning of stability test also exhibits a constant current as shown in Figure 4a, inset. The comparison between SEM images of electrode before any PEC test (as-synthesized sample), and after PEC tests and a long photocurrent stability test of over 6 h (**Figure 5**) show that there is no significant morphological changes with preservation of all materials within the css-NWs. The photoelectrochemical stability test of the Si/SnO_2/Fe_2O_3 css-NWs with Si(100) NW cores is shown in Supporting Information, Figure S5, in which there is no saturation behavior and constant current like that shown in Figure 4a for the css-NWs with Si(111) NWs. In fact, the photocurrent continuously increases with a small slope indicating the gradual and slow decomposition of Fe_2O_3 NCs. These observations reveal that the stability performance of the Si/SnO_2/Fe_2O_3 css-NWs is dependent on the p-Si surface orientation in which the css-NWs with p-Si(111) present higher stability because the p-Si(111) surface is more stable than p-Si(100) surface in aqueous solutions.[53,54] The investigation of Fe_2O_3 NCs grown on the SnO_2-coated p-Si wafers also showed that the photocathode samples with Si(111) exhibit a long-term stability without any significant Fe_2O_3 NCs morphology change or dissolution, which was not the case for the electrodes with p-Si(100). Note that despite not providing a constant photocurrent over long time, the starting of photocurrent stability test (0–20 min) for the Si(100)/SnO_2/Fe_2O_3 css-NWs exhibits a constant current (see Supporting Information, Figure S5, inset) further confirming the high PEC activity shown in the *J*–*V* measurements (which also shown using different current scans in Supporting Information, Figure S4) and disproofing the fact that dissolution of Fe_2O_3 may contribute to the *J*–*V* measurements. Moreover, the Si(100)/SnO_2/Fe_2O_3 css-NWs preserve their high photoactivity after several months by keeping them in vacuum (see Figure 4b). The cyclic voltammetry measurement on the Si(100)/SnO_2/Fe_2O_3 css-NWs (data not shown here) also showed that there is no corrosive peak.

To further evaluate the photocathodic performance of the Si/SnO_2/Fe_2O_3 css-NWs, their photocurrent and stability were compared to our previously reported ZnO/Si branched NWs and TiO_2/Pt-coated ZnO/Si branched NWs[36] that have almost similar core and shell dimensions (see Supporting Information, Figures S6 and S7). The Si/SnO_2/Fe_2O_3 css-NWs show higher photocathodic current and lower photocathodic turn-on potential than the ZnO/Si branched NWs. Moreover, they provide comparable long-term stability to that of the TiO_2/Pt-coated ZnO/Si branched NWs, while the ZnO/Si branched NWs cannot provide a long-term stability (see Supporting Information, Figure S7). Therefore, we emphasize that our achieved results for the Si/SnO_2/Fe_2O_3 css-NW photocathodes are promising considering several factors: (i) performance was evaluated in a neutral electrolyte with a low morality of 0.25, (ii) there is no any metal catalyst coating on the samples, and (iii) the css-NWs provide long-term stability without any need for the atomic-layer-deposition (ALD) passivation which is a costly technique.

3. Conclusions

In summary, we showed the fabrication of p-Si/n-SnO_2/n-Fe_2O_3 css-NW photocathodes using facile synthesis methods and their use for improved and durable solar water splitting in a neutral medium. The p-Si/SnO_2/Fe_2O_3 css-NW photocathodes exhibited considerably increased photocathodic photocurrent, lowered turn-on potential, and improved conversion efficiency, compared to that of the bare p-Si NW or p-Si/n-SnO_2 cs-NW photocathodes. The photoactivity at 0 V versus RHE and low onset potential for the css-NW photocathodes revealed the promising potential of overcoming the HER kinetics limitation at the surface of the p-Si photocathodes using metal oxides. More notably, the css-NW electrodes showed significant PEC stability of hours without any considerable morphological change. These results can pave the way to achieve overall solar water splitting in a full PEC system.

4. Experimental Section

Fabrication of Si/SnO_2/Fe_2O_3css-NW Electrodes: The boron doped Si(100) and Si(111) substrates with resistivities of 1–20 Ω cm (p-type) were patterned into 3D configurations with an array of Ni disk masks prepared using nanoimprint lithography and e-beam evaporation.[26] The Reactive Ion Etching-Inductively Coupled Plasma (RIE-ICP) dry etching was used to make vertical Si NW arrays for different diameters and lengths by etching for various times with Ni disks serving as the etch mask. The average Si(100) etching rate was ≈0.24 μm min^{-1}. Note that for p-Si(111) samples, the newly used mold for nanoimprinting had a little larger diameter so the etching rate was ≈0.27 μm min^{-1} for these samples. The pitch size (center-to-center spacing) of Si NW array was 1 μm for both Si(100) and Si(111) samples. After the RIE-ICP etching, the Si NW substrates were dipped into Ni etchant for 5 min to etch/remove the Ni disks at the head of Si NWs. The Si NW substrates were then cleaned with RCA cleaning to remove the contamination from the RIE-ICP etching. Afterwards, the Si NW samples were immediately transferred to the sputtering machine to deposit a thin SnO_2 layer, as seeding layer for the Fe_2O_3 NCs shell growth, using RF magnetron sputtering with 99.99% SnO_2 target and argon gas at room temperature. The RF power was 400 W during the sputtering deposition. SnO_2 is

physisorbed on the Si surface in the Si NW samples by mechanisms of hydroxyl group bonding and van der Waals force. Hydroxyl comes from the RCA cleaning and even humidity or water. The SnO_2 layer uniformly covered the Si NWs due to substrate rotation during the sputtering deposition. The uniform SnO_2 deposition is evident with uniform growth of the Fe_2O_3 NCs on the Si NWs as well as on the flat surface between the Si NWs due to the fact that without the SnO_2 seeding layer, there is no Fe_2O_3 growth, which we tested it. The actual thickness of sputtered SnO_2 seeding layer on the 10m-Si NWs was ≈28 nm according to the high-magnification SEM images. Finally, the Fe_2O_3 NCs were grown on the SnO_2-coated Si NW cores using hydrothermal growth method.[40,42] First, akaganeite (β-FeOOH) NCs were grown on the SnO_2-coated Si NW trunks as follows. The SnO_2-coated Si NW substrate was put in a 45 mL sealed Teflon autoclave containing a 30 mL aqueous solution consisting of 0.15 M $FeCl_3.6H_2O$ (Iron(III) chloride hexahydrate) (Sigma-Aldrich, ≥99%) and 1 M $NaNO_3$ (sodium nitrate) (Sigma-Aldrich, ≥99.0%). The deionized (DI) water resistivity and pH of growth solution were 17.6–17.7 MΩ cm and ≈1.44, respectively. The hydrothermal reaction was performed at a temperature of ≈107 °C, putting the autoclave in a regular oven, for the desirable growth time. The as-prepared sample was then rinsed carefully with DI water to remove the residues and dried with N_2 flow. After the FeOOH NC growth, the color of Si NW substrate turned into yellowish indicating the FeOOH growth. Finally, the as-grown Si/SnO_2/FeOOH css-NW substrates were annealed at 450 °C under air (in an open furnace) for 2 h to have phase transition from the β-FeOOH to (α-Fe_2O_3. The yellowish color of substrate turned into reddish color showing the transformation of β-FeOOH into α-Fe_2O_3.

Structural Characterization: A Philips XL30 field-emission environmental scanning electron microscope (ESEM) working at an accelerating voltage of 10.0 kV was used for examining the samples morphologies. A high resolution transmission electron microscopy (HRTEM, JEOL JEM3100F) operated at 300 kV was used for the atomic-scale structural analyses. Spherical aberration-corrected scanning transmission electron microscopy (Cs-corr. STEM, JEOL JEM2100F) operated at 200 kV was also employed for further studies and to identify the actual atomic configuration of NWs. High resolution energy dispersive X-ray spectroscopy (EDS, EDAX) was performed to obtain the elemental information on individual layers within the css-NW.

Photoelectrochemical (PEC) Measurements: To perform the PEC tests, the samples were bonded to Cu wire at the back using indium, which provides an ohmic contact. The edges and backside of samples were sealed using epoxy. Current density (*J–V* and *J–t*) measurements were carried out in a 400 mL aqueous solution of 0.25 M Na_2SO_4 buffered at pH = 7.25 with Phosphate Buffered Saline (PBS, Sigma) (DI water resistivity, 17.6–17.7 MΩ cm) (neutral solution) with a three-electrode configuration, including sample as working electrode (WE), Pt mesh as counter electrode (CE), and Ag/AgCl (1 M KCl) as reference electrode (RE). For the *J–V* measurements in an electrolyte with a pH of 13.5, a 400 mL aqueous solution of 1 M NaOH was used. A light power intensity of 100 mW cm^{-2} was adjusted at the samples position provided by a solar simulator (Newport 67015) using a 150 W Xenon lamp and equipped with a 1.5 AM filter. The current density measurements were collected using a potentiostat (Digi-Ivy Inc). A scan rate of 10 mV s^{-1} was employed for the linear sweep voltammetry (LSV) (*J–V* measurements). Photocurrent stability tests were carried out by collecting the electrodes current under a fixed illumination of 100 mW cm^{-2} and at a biasing potential of –0.33 V versus reversible hydrogen electrode (RHE). During the current density measurements, a mild agitation was employed and the electrolyte was constantly purged with a small flow of N_2 gas. The biasing potentials versus Ag/AgCl RE ($E_{Ag/AgCl}$) were converted to the potentials versus RHE, E_{RHE}, using the Nernst equation

$$E_{RHE} = E_{Ag/AgCl} + 0.059\text{pH} + E^0_{Ag/AgCl} \quad \text{(V)} \tag{1}$$

where pH is the electrolyte pH (7.25 or 13.5 here) and $E^0_{Ag/AgCl}$ = 0.236 V for the Ag/AgCl RE in 1 M KCl and at 25 °C. The current densities here are calculated using geometric areas.

Supporting Information

Supporting Information is available from the Wiley Online Library or from the author.

Acknowledgements

D.W. acknowledges the financial support by the Department of Energy (DOE DE-FG36–08G018016) and the National Science Foundation (NSF ECCS0901113 and CBET1236155) for this work. D.W. thanks Drs. Ramesh Rao and Bernd Fruhberger of QI for their unconditional support. A.K. acknowledges Larry Grissom, Sean Park, Ivan Harris, Matthew Sirriyeh, and Steve Schank of UCSD NANO3 facilities for their professional support. A.K. also acknowledges useful discussion with Prof. Shadi A. Dayeh from UCSD on the band diagram. TEM and STEM characterizations at the University of Michigan are supported as part of the Center for Solar and Thermal Energy Conversion, an Energy Frontier Research Center funded by the U.S. Department of Energy, Office of Science, Office of Basic Energy Sciences under Award Number DE-SC0000957. G.Y.J. was supported by the Basic Research Program through the National Research Foundation of Korea (NRF) funded by the Ministry of Science, ICT and Future Planning (No. R15–2008–006–03002–0, CLEA, NCRC).

Received: December 25, 2014
Revised: February 21, 2015
Published online: March 21, 2015

[1] A. I. Hochbaum, P. Yang, *Chem. Rev.* **2009**, *110*, 527.
[2] J. Oh, H.-C. Yuan, H. M. Branz, *Nat. Nanotechnol.* **2012**, *7*, 743.
[3] H.-P. Wang, T.-Y. Lin, C.-W. Hsu, M.-L. Tsai, C.-H. Huang, W.-R. Wei, M.-Y. Huang, Y.-J. Chien, P.-C. Yang, C.-W. Liu, L.-J. Chou, J.-H. He, *ACS Nano* **2013**, *7*, 9325.
[4] J. Zhu, C.-M. Hsu, Z. Yu, S. Fan, Y. Cui, *Nano Lett.* **2009**, *10*, 1979.
[5] J. R. Maiolo, B. M. Kayes, M. A. Filler, M. C. Putnam, M. D. Kelzenberg, H. A. Atwater, N. S. Lewis, *J. Am. Chem. Soc.* **2007**, *129*, 12346.
[6] M. G. Walter, E. L. Warren, J. R. McKone, S. W. Boettcher, Q. Mi, E. A. Santori, N. S. Lewis, *Chem. Rev.* **2010**, *110*, 6446.
[7] J. Oh, T. G. Deutsch, H.-C. Yuan, H. M. Branz, *Energy Environ. Sci.* **2011**, *4*, 1690.
[8] S. K. Cho, F.-R. F. Fan, A. J. Bard, *Angew. Chem. Int. Ed.* **2012**, *51*, 12740.
[9] S. W. Boettcher, J. M. Spurgeon, M. C. Putnam, E. L. Warren, D. B. Turner-Evans, M. D. Kelzenberg, J. R. Maiolo, H. A. Atwater, N. S. Lewis, *Science* **2010**, *327*, 185.
[10] Y. Lin, C. Battaglia, M. Boccard, M. Hettick, Z. Yu, C. Ballif, J. W. Ager, A. Javey, *Nano Lett.* **2013**, *13*, 5615.
[11] K. Peng, X. Wang, S.-T. Lee, *Appl. Phys. Lett.* **2008**, *92*, 163103.
[12] A. Kargar, K. Sun, S. J. Kim, D. Lu, Y. Jing, Z. Liu, X. Pan, D. Wang, *Phys. Status Solidi A* **2013**, *210*, 2561.
[13] I. Oh, J. Kye, S. Hwang, *Nano Lett.* **2011**, *12*, 298.
[14] K. Sun, Y. Jing, C. Li, X. Zhang, R. Aguinaldo, A. Kargar, K. Madsen, K. Banu, Y. Zhou, Y. Bando, Z. Liu, D. Wang, *Nanoscale* **2012**, *4*, 1515.
[15] X. Wang, K.-Q. Peng, X.-J. Pan, X. Chen, Y. Yang, L. Li, X.-M. Meng, W.-J. Zhang, S.-T. Lee, *Angew. Chem. Int. Ed.* **2011**, *50*, 9861.
[16] Y. J. Hwang, C. H. Wu, C. Hahn, H. E. Jeong, P. Yang, *Nano Lett.* **2012**, *12*, 1678.
[17] M. T. Mayer, C. Du, D. Wang, *J. Am. Chem. Soc.* **2012**, *134*, 12406.
[18] C. Cheng, H. J. Fan, *Nano Today* **2012**, *7*, 327.
[19] M. J. Bierman, S. Jin, *Energy Environ. Sci.* **2009**, *2*, 1050.
[20] R. N. Dominey, N. S. Lewis, J. A. Bruce, D. C. Bookbinder, M. S. Wrighton, *J. Am. Chem. Soc.* **1982**, *104*, 467.

[21] S. W. Boettcher, E. L. Warren, M. C. Putnam, E. A. Santori, D. Turner-Evans, M. D. Kelzenberg, M. G. Walter, J. R. McKone, B. S. Brunschwig, H. A. Atwater, N. S. Lewis, *J. Am. Chem. Soc.* **2011**, *133*, 1216.
[22] E. L. Warren, J. R. McKone, H. A. Atwater, H. B. Gray, N. S. Lewis, *Energy Environ. Sci.* **2012**, *5*, 9653.
[23] J. R. McKone, E. L. Warren, M. J. Bierman, S. W. Boettcher, B. S. Brunschwig, N. S. Lewis, H. B. Gray, *Energy Environ. Sci.* **2011**, *4*, 3573.
[24] S. Y. Reece, J. A. Hamel, K. Sung, T. D. Jarvi, A. J. Esswein, J. J. H. Pijpers, D. G. Nocera, *Science* **2011**, *334*, 645.
[25] Y. W. Chen, J. D. Prange, S. Dühnen, Y. Park, M. Gunji, C. E. D. Chidsey, P. C. McIntyre, *Nat. Mater.* **2011**, *10*, 539.
[26] A. Kargar, K. Sun, Y. Jing, C. Choi, H. Jeong, Y. Zhou, K. Madsen, P. Naughton, S. Jin, G. Y. Jung, D. Wang, *Nano Lett.* **2013**, *13*, 3017.
[27] Y. J. Hwang, A. Boukai, P. Yang, *Nano Lett.* **2009**, *9*, 410.
[28] K. Jun, Y. S. Lee, T. Buonassisi, J. M. Jacobson, *Angew. Chem. Int. Ed.* **2012**, *51*, 423.
[29] N. C. Strandwitz, D. J. Comstock, R. L. Grimm, A. C. Nichols-Nielander, J. Elam, N. S. Lewis, *J. Phys. Chem. C* **2013**, *117*, 4931.
[30] K. Sun, X. Pang, S. Shen, X. Qian, J. S. Cheung, D. Wang, *Nano Lett.* **2013**, *13*, 2064.
[31] H. P. Maruska, A. K. Ghosh, *Sol. Energy Mater.* **1979**, *1*, 411.
[32] P. A. Kohl, S. N. Frank, A. J. Bard, *J. Electrochem. Soc.* **1977**, *124*, 225.
[33] G. Hodes, L. Thompson, J. DuBow, K. Rajeshwar, *J. Am. Chem. Soc.* **1983**, *105*, 324.
[34] K. H. Yoon, D. K. Seo, Y. S. Cho, D. H. Kang, *J. Appl. Phys.* **1998**, *84*, 3954.
[35] X. Lu, T. Minegishi, J. Kubota, K. Domen, *Jpn. J. Appl. Phys.* **2011**, *50*, 085702.
[36] A. Kargar, K. Sun, Y. Jing, C. Choi, H. Jeong, G. Y. Jung, S. Jin, D. Wang, *ACS Nano* **2013**, *7*, 9407.
[37] K. Sivula, F. Le Formal, M. Grätzel, *ChemSusChem* **2011**, *4*, 432.
[38] S. C. Warren, E. Thimsen, *Energy Environ. Sci.* **2012**, *5*, 5133.
[39] S. C. Warren, K. Voïtchovsky, H. Dotan, C. M. Leroy, M. Cornuz, F. Stellacci, C. Hébert, A. Rothschild, M. Grätzel, *Nat. Mater.* **2013**, *12*, 842.
[40] L. Vayssieres, N. Beermann, S.-E. Lindquist, A. Hagfeldt, *Chem. Mater.* **2001**, *13*, 233.
[41] Y. Ling, G. Wang, J. Reddy, C. Wang, J. Z. Zhang, Y. Li, *Angew. Chem. Int. Ed.* **2012**, *51*, 4074.
[42] W. Zhou, C. Cheng, J. Liu, Y. Y. Tay, J. Jiang, X. Jia, J. Zhang, H. Gong, H. H. Hng, T. Yu, H. J. Fan, *Adv. Funct. Mater.* **2011**, *21*, 2439.
[43] M. P. Dare-Edwards, J. B. Goodenough, A. Hamnett, P. R. Trevellick, *J. Chem. Soc., Faraday Trans. 1* **1983**, *79*, 2027.
[44] J. H. Kennedy, K. W. Frese, *J. Electrochem. Soc.* **1978**, *125*, 709.
[45] K. Itoh, J. O. M. Bockris, *J. Electrochem. Soc.* **1984**, *131*, 1266.
[46] N. J. Cherepy, D. B. Liston, J. A. Lovejoy, H. Deng, J. Z. Zhang, *J. Phys. Chem. B* **1998**, *102*, 770.
[47] A. J. Bosman, H. J. van Daal, *Adv. Phys.* **1970**, *19*, 1.
[48] C. Sanchez, K. D. Sieber, G. A. Somorjai, *J. Electroanal. Chem.* **1988**, *252*, 269.
[49] N. Iordanova, M. Dupuis, K. M. Rosso, *J. Chem. Phys.* **2005**, *122*, 144305.
[50] F. Le Formal, N. Tetreault, M. Cornuz, T. Moehl, M. Gratzel, K. Sivula, *Chem. Sci.* **2011**, *2*, 737.
[51] T. K. Townsend, E. M. Sabio, N. D. Browning, F. E. Osterloh, *Energy Environ. Sci.* **2011**, *4*, 4270.
[52] A. Kargar, J. S. Cheung, C.-H. Liu, T. K. Kim, C. T. Riley, S. Shen, Z. Liu, D. J. Sirbuly, D. Wang, S. Jin, *Nanoscale* **2015**, *7*, 4900.
[53] K. Sakaino, S. Adachi, *J. Electrochem. Soc.* **2002**, *149*, G543.
[54] P. M. M. C. Bressers, J. J. Kelly, J. G. E. Gardeniers, M. Elwenspoek, *J. Electrochem. Soc.* **1996**, *143*, 1744.